Draft version August 17, 2022
Typeset using LaTeX default style in AASTeX61

EFFECTS OF SPECTRAL RESOLUTION ON SIMPLE MAGNETIC FIELD DIAGNOSTICS OF THE MG II H & K LINES

Rebecca Centeno,[1] Matthias Rempel,[1] Roberto Casini,[1] and Tanausú del Pino Alemán[2]

[1] *High Altitude Observatory (NCAR), 3080 Center Green Dr., Boulder, CO, USA*
[2] *Instituto de Astrofísica de Canarias, C/ Vía Láctea S/N, 38204 La Laguna, Spain*

(Received July 1, 2016; Revised September 27, 2016; Accepted August 17, 2022)

Submitted to ApJ

ABSTRACT

We study the effects of finite spectral resolution on the magnetic field values retrieved through the weak field approximation (WFA) from the cores of the Mg II h&k lines. The retrieval of the line-of-sight (LOS) component of the magnetic field, $B_{\rm LOS}$, from synthetic spectra generated in a uniformly magnetized FAL-C atmosphere are accurate when restricted to the inner lobes of Stokes V. As we degrade the spectral resolution, partial redistribution (PRD) effects that more prominently affect the outer lobes of Stokes V, are brought into the line core through spectral smearing, degrading the accuracy of the WFA and resulting in an inference bias, which is more pronounced the poorer the resolution. When applied to a diverse set of spectra emerging from a sunspot simulation, we find a good accuracy in the retrieved $B_{\rm LOS}$ when comparing it to the model value at the height where the optical depth in the line core is unity. The accuracy is preserved up to field strengths of B$\sim$1500 G. Limited spectral resolution results in a small bias toward weaker retrieved fields. The WFA for the transverse component of the magnetic field is also evaluated. Reduced spectral resolution degrades the accuracy of the inferences because spectral mixing results in the line effectively probing deeper layers of the atmosphere.

Keywords: solar magnetic fields

Corresponding author: Rebecca Centeno
rce@ucar.edu

1. INTRODUCTION

Inference of the photospheric magnetic field vector has been routinely carried out from ground-based observatories for decades. With the advent of spectropolarimeters in space, these observations (and their interpretation in terms of the vector magnetic field) have reached the consistent (and continuous) high data quality required for precise analysis of the magnetic field evolution. While the HMI instrument (Scherrer et al. 2012) on board the Solar Dynamics Observatory (Pesnell et al. 2012) provides full disk measurements at good cadence and moderate spatial resolution, the Hinode spectro-polarimeter (Kosugi et al. 2007; Lites et al. 2013) offers a higher-resolution counterpart within a much smaller FOV and limited temporal cadence. The Solar Orbiter PHI instrument (Solanki et al. 2020) will soon bring the first ever magnetic field measurements at the solar poles with significant less foreshortening than observations made from the ecliptic plane. While each one of these observational benchmarks has furthered our knowledge of the Sun's magnetism in a step-wise manner, the inferred magnetic field is still confined to a thin atmospheric layer next to the Sun's surface.

Between the dynamically driven photosphere and the magnetically dominated corona, lies the ever-elusive chromosphere, where the transition from the high- to low-β regime takes place. This interface region is also the connective tissue between the Sun's surface and its outer envelope. The coronal heating conundrum manifests indeed in the chromosphere, where the radiative losses due to its proximity to outer space need to be compensated by efficient heating mechanisms; and magnetic reconnection is a promising candidate to explain said heating (see, for instance, the discussion in Lagg et al. 2017).

Chromospheric magnetometry is challenging at many levels, from the limits imposed by instrument sensitivity to the complexity of the interpretation of the observations. Ground-based observations of magnetically-sensitive chromospheric spectral lines (most notably He I 10830 Å, Ca II 8542 Å and He I D3 at 5876 Å) have started to bridge the knowledge gap of what happens in this interface region (e.g. Morosin et al. 2020; Libbrecht et al. 2019; Kleint 2017; Martínez González et al. 2015; Centeno et al. 2010; Merenda et al. 2006, among many others!). Trujillo Bueno et al. (2017) make a case for spectropolarimetric observations in the ultraviolet part of the spectrum for probing the magnetic field in the upper chromosphere and the transition region. Due to their high line core opacity as well as the relative brightness of the UV spectral range where they sit, the Mg II resonance lines at 280 nm are considered to be excellent probes, not only of the thermodynamics (Leenaarts et al. 2013a,b), but also the magnetic conditions in the high chromosphere (del Pino Alemán et al. 2016; Alsina Ballester et al. 2016; Manso Sainz et al. 2019; Judge et al. 2021).

Leading up to the launch of the Interface Region Imaging Spectrograph (IRIS De Pontieu et al. 2014), a series of papers analyzed the properties and modeling requirements of Mg II h&k. Leenaarts et al. (2013a) determined the minimum atomic model necessary to reproduce the intensity spectrum of these lines, and studied the effects of 1D vs 3D radiative transfer modeling, and including vs ignoring the effects of partial frequency redistribution (PRD). In a followup paper, Leenaarts et al. (2013b) carried out a detailed study of the morphological properties of Mg II h&k intensity profiles and their correlation with the thermodynamical properties in the numerical simulation used to generate them. They found that the positions and relative amplitudes of the spectral features serve as proxies of the velocity and the temperature in the higher layers of the chromosphere. Even after applying spectral and spatial smearing to the synthetic data, some of these inferences remain robust (Pereira et al. 2013). de la Cruz Rodríguez et al. (2016) show that non-LTE inversions of the spectral line intensity allow for the retrieval of the full temperature stratification from the mid-photosphere all the way up to the transition region, whilst the velocity gradients can be estimated throughout the chromosphere. This is a rather computationally demanding approach, however, and for this reason, Sainz Dalda et al. (2019) developed a machine-learning approach that speeds up traditional inversion methods by a factor of $10^5 - 10^6$, while still reproducing the thermodynamical state of the atmosphere with comparable quality to traditional minimization-based techniques.

The IRIS observations, however, only measure the intensity of the Mg II lines. Measuring the spectral line polarization would open up the possibility of magnetic field diagnostics in this crucial interface region at the base of the corona. In a renewed attempt to analyze spectropolarimetric observations of Mg II resonance lines from the Ultraviolet Spectrometer and Polarimeter on board the Solar Maximum Mission (SMM, Bohlin et al. 1980), Manso Sainz et al. (2019) confirmed that the magnetograph formula can be applied to observations of the circular polarization in the line core. They obtained line-of-sight magnetic fields of the order of 500 G from these observations. The authors also report on observational evidence of reduction of the broad-band linear polarization with respect to the field-free case due to weak magnetic fields outside of active regions. This had been theoretically predicted by del Pino Alemán et al. (2016)

and Alsina Ballester et al. (2016) and presents a promising diagnostic for the weaker chromospheric fields of the quiet Sun.

Decades after the SMM first measured the polarization of the Mg II UV doublet, the 2019 launch of the Chromospheric LAyer Spectropolarimeter (CLASP2, Ishikawa et al. 2021) revisited this part of the spectrum with very promising findings. The circular polarization profiles of h&k in a plage region away from disk center were interpreted using the weak field approximation (WFA) and revealed longitudinal magnetic fields of up to $\sim$ 300 G at the top of the chromosphere, while a nearby Mn I multiplet provided simultaneous information for lower layers.

Outside of active regions, the linear polarization in the core of Mg II k (as well as the surrounding broad-band polarization) is expected to be dominated by scattering phenomena. Trying to interpret these non-Zeeman signatures via the WFA relations would lead to erroneous inferences. Furthermore, most currently available non-LTE spectral line inversion codes do not model the quantum-mechanical processes responsible for scattering polarization and the Hanle effect, also rendering them inadequate for the interpretation of these signals (see Centeno et al. 2021, for an analysis of this effect in Ca II 8542 Å)). The newly published Tenerife Inversion Code (TIC, Li et al. 2022) is the first of its kind able to tackle scattering polarization and Hanle-effect signatures in the Mg II resonance lines. This is advancement will enable detailed interpretation of the spectra, but comes at large computational cost and can only be used sparingly[1].

While scattering polarization signals dominate the linear polarization in and around the Mg II doublet (except for the core of the h line, see del Pino Alemán et al. 2016; Casini et al. 2002), the core of Stokes V remains agnostic to these effects (del Pino Alemán, private communication), allowing for a Zeeman interpretation of the LOS component of the magnetic field. In the presence of stronger fields, even the linear polarization becomes dominated by the Zeeman effect, and retrieval methods based on it should in principle still work. In this paper, we study the error incurred by the WFA when applied to the Mg II h & k lines to obtain magnetic field inferences from synthetic spectra emerging from an active region simulation. In particular, we look at how spectral resolution degrades the accuracy of the results. Section 2 presents a brief overview of the WFA as well as the radiative transfer code (Hanle-RT) that enables the spectral synthesis. We first explore the effects of spectral resolution on the WFA applied to spectra emerging from a standard semi-empirical model atmosphere (Section 3), and then in Section 4 we take the analysis to a more diverse set of spectra emerging from a radiative magneto-hydrodynamic (rMHD) simulation of an active region. We discuss the feasibility of the method and draw some concluding remarks in Section 5.

2. METHODOLOGY

2.1. *The Weak Field Approximation*

The weak field approximation (WFA; e.g. Landi Degl'Innocenti & Landolfi 2004) is a simple, yet relatively robust method, to extract magnetic field information from the intensity and polarization of spectral lines. As its name suggests, its validity is limited to the "weak" field regime, or more precisely, to the range of field strengths (B) in which the Zeeman-splitting ($\Delta\lambda_{\rm B}$) of the spectral line is much smaller than its Doppler width, $\Delta\lambda_{\rm D}$:

$$\bar{g}\frac{\Delta\lambda_{\rm B}}{\Delta\lambda_{\rm D}} << 1 \tag{1}$$

where $\bar{g}$ is the effective Landé factor of the spectral line and the Zeeman splitting is proportional to the magnetic field strength (B, in gauss) and the square of the central wavelength of the spectral line under consideration (λ_0, in Å):

$$\bar{g}\Delta\lambda_{\rm B} = 4.67\times10^{-13}\bar{g}\lambda_0^2 B \tag{2}$$

When applying a perturbative scheme to the radiative transfer equation in this regime, one arrives at a series of relations that connect the circular and the linear polarization spectra to derivatives of the intensity with respect to wavelength. Eq. 3 relates Stokes V to the first derivative of Stokes I with respect to wavelength, through the line-of-sight (LOS) component of the magnetic field vector, $B_{\rm LOS}$, and a constant $C_{\parallel}$ that depends on atomic properties of the spectral line.

$$V(\lambda) = -C_{\parallel}B_{\rm LOS}\frac{\partial I}{\partial\lambda} \tag{3}$$

[1] The computational expense of inverting a single spectrum is of the order of 1000 core-hours.

Eqs. 4 and 5, on the other hand, relate the total linear polarization ($L = \sqrt{Q^2 + U^2}$) to the derivative of Stokes I through the square of the transverse component of the magnetic field vector, $B_{\rm T}^2$, and a different constant, C_T, that also depends on properties intrinsic to the spectral line:

$$L(\lambda_w) = \frac{3}{4} B_T^2 \left| C_T \frac{1}{\lambda_w - \lambda_0} \right| \left| \frac{\partial I}{\partial \lambda} \right|_{\lambda_w} \tag{4}$$

$$L(\lambda_0) = \frac{1}{4} B_T^2 \left| C_T \frac{\partial^2 I}{\partial \lambda^2} \right|_{\lambda_0} \tag{5}$$

where the first of these two equations is applicable only in the line wing (λ_w) and the latter in the line core (close to the central wavelength, λ_0). The derivation of these relations as well as the conditions for their applicability can be found in Landi Degl'Innocenti & Landolfi (2004).

The WFA has been used in many works to extract quantitative information of the magnetic field vector from spectropolarimetric observations (see, for instance, Kriginsky et al. 2021; Vissers et al. 2021; Siu-Tapia et al. 2020; Shchukina & Trujillo Bueno 2019, for some recent applications of the WFA). Chromospheric spectral lines tend to satisfy the WFA requirement of Eq. 1 for larger field strengths than their photospheric counterparts owing to the fact that they are typically much wider than the latter. Additionally, lines that sit in the ultraviolet part of the spectrum enjoy smaller Zeeman splittings due to their shorter wavelengths, and lighter atomic species also meet the weak field requirement better, since they typically experience larger Doppler broadenings than their heavier counterparts.

The circular polarization of the Mg II resonance lines is known to be amenable to the WFA (del Pino Alemán et al. 2016), and given strong enough fields, their linear polarization signals may be interpreted with it as well.

2.2. *Spectral synthesis*

Hanle-RT (see del Pino Alemán et al. 2016, for a more comprehensive description) is a non-LTE polarized radiative transfer code for 1-D (plane-parallel) stratified atmospheres. It accepts any multi-level or multi-term atom (LS-coupling scheme) without hyperfine structure and in the presence of magnetic fields of arbitrary strength. The code takes into account the effects of non-isotropic radiative excitation of the atomic system, which are responsible for the manifestation of scattering polarization. Therefore, the code can model seamlessly all possible regimes of magnetic-induced effects on the polarization of spectral lines: the Hanle, Zeeman, and (incomplete) Paschen-Back effects, as well as the polarization effects associated with level crossing and anti-crossing interference. The code takes into account the effects of inelastic and elastic collisions, and also includes a comprehensive description of partially coherent scattering (partial redistribution, or PRD) from polarized atoms (limited to 3-term atoms of the Λ-type; see Casini & Manso Sainz 2016), which is important for modeling deep chromospheric lines.

The atomic model of Mg II used to solve the statistical equilibrium (SE) includes 3 terms of the singly-ionized species as well as the ground term of Mg III. This is the smallest atomic model necessary to model the atomic level polarization of the Mg II UV doublet around 280 nm as well as its subordinate triplet overlapping in the same wavelength range. The UV doublet is treated in PRD whilst the subordinate triplet is computed assuming complete frequency redistribution.

3. MODELING IN A FAL-C ATMOSPHERE

We first synthesize the Mg II h & k lines in the standard 1-D FAL-C (Fontenla et al. 1990) semi-empirical model of the Sun's atmosphere with an ad-hoc uniform magnetic field of 200 G inclined 45° with respect to the local solar vertical. For a disk center observing geometry, this configuration results in a LOS component of the magnetic field of $B_{\rm LOS} \approx 141$ G. A uniform magnetic field is chosen in order to isolate the WFA inference error from other radiative transfer effects resulting from LOS integration. Fig. 1 shows the synthetic spectrum including the Mg II resonance lines as well as the subordinate triplet. Three different syntheses are computed in this model atmosphere: the first one is a full Hanle-RT calculation; in the second one we turn off magneto-optical effects; and in the third one we turn off PRD effects instead.

We then apply Eq. 3 by carrying out a linear regression ($y_i = a \cdot x_i + b$) of the data to determine the slope a and the intercept b. Here, y_i correspond to the values of V_λ, while x_i are taken to be the values of $-C_\parallel dI_\lambda/d\lambda$, with the proportionality between the two given by the fitted slope ($a = B_{\rm LOS}$), and a fitted intercept b that should be compatible with zero. Because the WFA is just an approximation, the linear relationship between V_λ and $dI_\lambda/d\lambda$ does not hold outside of the Zeeman weak field assumption. When the data don't meet the criteria for the WFA (and the

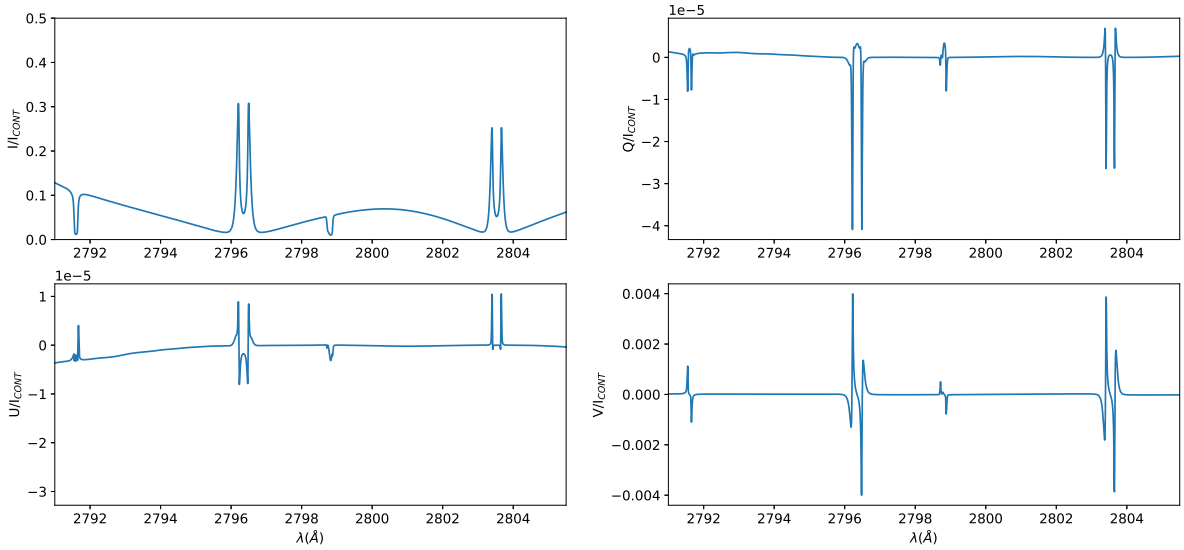

Figure 1. Mg II h & k as well as the subordinate UV triplet lines synthesized in a FAL-C model atmosphere with a magnetic field strength of $B = 200$ G inclined 45° from the local vertical, as if observed at disk center. Note the double lobes of the Stokes V profiles for the h & k lines. The x-axis represents vacuum wavelengths, and Mg II k sits around 2796.3 Å.

relationship is no longer linear), the linear fit might yield an intercept that is not compatible with zero, and a slope that is wrongly interpreted as $B_{\rm LOS}$.

Fig. 2 shows the WFA fit for the LOS component of the magnetic field applied to the three synthetic profiles of Mg II k. The blue dots represent the values of Stokes V (rearranged as a function of increasing wavelength and normalized by the local continuum intensity), while the orange line shows the derivative of Stokes I with respect to wavelength, scaled by $C_{\|}B_{\rm LOS}$, where $B_{\rm LOS}$ was obtained from a linear regression applied to Eq. 3. The relative error incurred by the WFA is reported for each case inside the corresponding panel. In the case where the WFA is applied to the inner lobes of Stokes V only (top row) the inference error is 1.4% when the line is treated in PRD (left and middle panels), compared to 0.1% in the scenario where PRD is turned off (right panel). However, when the outer lobes are taken into account in the linear regression (bottom row), the inference errors jump to −13% in the two PRD cases (bottom left and middle panels), which is also evidenced by the poor quality of the fit. When PRD is turned off, the error is still very small (bottom right) and the retrieved $B_{\rm LOS}$ produces a good fit. This shows that the inaccuracy incurred by the WFA is mostly due to PRD effects and can be avoided by excluding the outer Stokes V lobes from the calculation. On the other hand, magneto-optical effects alone (for this regime of field strengths) do not have negative impacts on the WFA retrieval of $B_{\rm LOS}$[2].

In CRD, the WFA corresponds to the lowest-order result of a perturbative solution of the polarized radiative transfer equation in the presence of a magnetic field (Landi Degl'Innocenti & Landi Degl'Innocenti 1973). In PRD, however, the emissivity vector ϵ gets modified by a redistribution correction $\delta\epsilon$ (see, e.g. Casini et al. 2017), which breaks the symmetry of such a perturbative solution, and is ultimately responsible for the observed departure of the validity of the WFA in PRD away from the line core. We believe this is the only plausible physical mechanism that can be responsible for the WFA breaking down away from the line core.

3.1. *Effects of spectral resolution*

Most instruments that observe solar spectral lines have limited spectral resolution. Spectral smearing mixes information across the wavelength domain, possibly bringing information from the line wings into the line core, and vice-versa. For the WFA, this means that information captured by the line wings (which "sense" magnetic fields at

[2] according to Landi Degl'Innocenti & Landolfi (2004), M-O effects yield corrections of the order of $(\Delta\lambda_B/\Delta\lambda_D)^4$ for the derivation of the LOS magnetic field from the WFA (pp. 488-489).

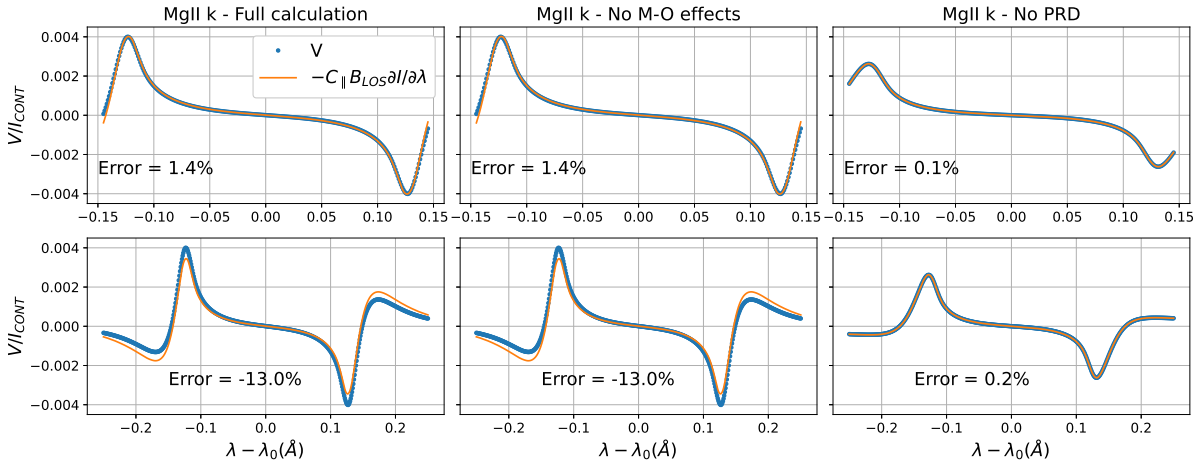

Figure 2. WFA fit of Stokes V for Mg II k for the cases where the spectra were synthesized with no approximations (left), when magneto-optical effects were turned off (middle) and when no PRD effects were considered (right). The top row corresponds to the WFA applied on the inner lobes of Stokes V only, whilst the bottom row applies the equation to both sets of lobes. The error incurred by the WFA is reported inside each panel.

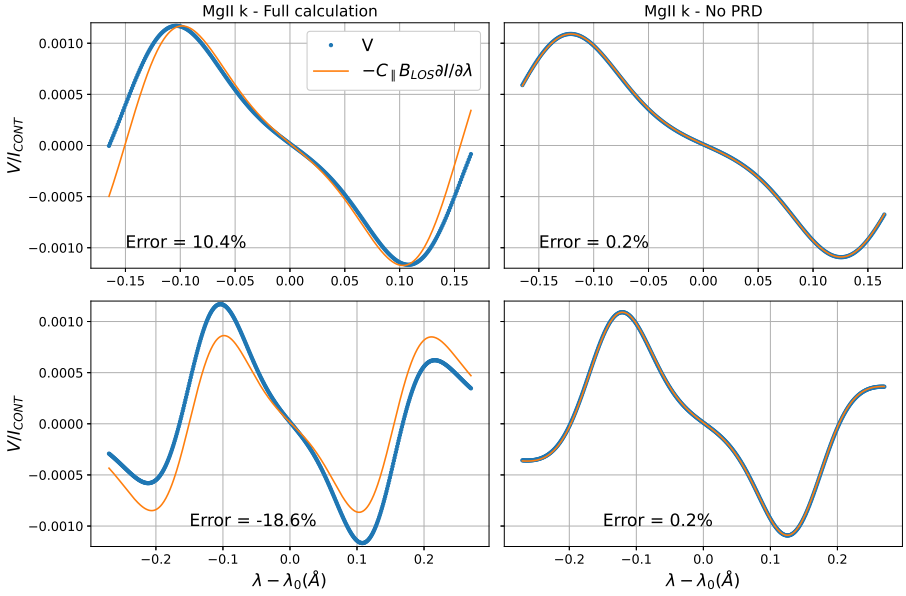

Figure 3. Application of the WFA fit (orange) to Mg II k Stokes V spectra (blue) that have been previously degraded with a gaussian point spread function corresponding to a spectral resolution of R = 30,000. In the top row, the WFA has been applied to the inner lobes of Stokes V only, whilst the bottom panels show the results when applied to a wider wavelength range. PRD effects in the full calculation (left) result in large inference errors that are not present when PRD is turned off (right).

lower atmospheric heights) may be dragged into the core of the line, resulting in line-of-sight smearing of the retrieved magnetic quantities. But even when the magnetic field is constant with height, the PRD effects that are prominent in the outer lobes of Stokes V can be partially transferred to the inner lobes, and "contaminate" the WFA inference applied to the narrower spectral range.

In order to quantify the latter effect, we apply gaussian point spread functions (PSF) of different widths to the synthetic spectra described above, and apply the WFA to the inner lobes of Stokes V in the degraded spectra. Because the spectral syntheses were carried out in an atmosphere with a uniform magnetic field, the line-of-sight smearing of the retrieved magnetic properties is inconsequential.

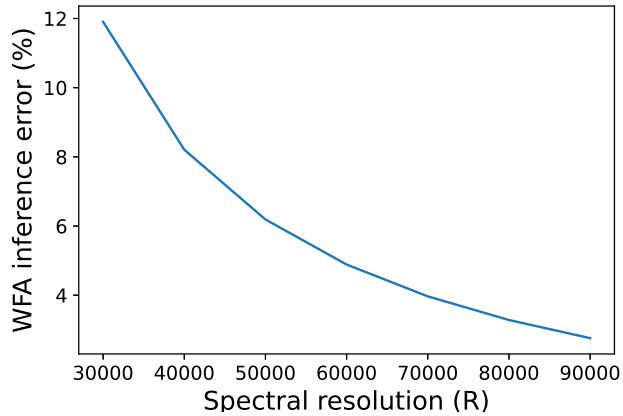

Figure 4. Error incurred by the WFA when inferring for $B_{\rm LOS}$ from the Mg II k line as a function of spectral resolution. The WFA was applied to the inner lobes of Stokes V only.

The top left panel of Fig. 3 shows the WFA fit (orange lines) for Mg II k applied to the inner lobes of Stokes V (blue dots) in the case of the full calculation with PRD and a spectral resolution of R = 30,000 (which is approximately the spectral resolution of the CLASP II observations). The relative error in the retrieved $B_{\rm LOS}$ is $\sim 10.4\%$. Including the outer Stokes V lobes in the WFA inference (bottom left) drives the relative inference error to -18%. On the other hand, when PRD is turned off (right panels), the inference error remains very low (0.2%) in both cases. This example epitomizes how the PRD effects that are prominent in the outer lobes, are brought into the inner lobes due to spectral smearing, negatively impacting the WFA inference.

Fig. 4 shows the relative error of the WFA results for $B_{\rm LOS}$ as a function of spectral resolution of the observations. As expected, smaller values of R result in greater retrieval errors. It is important to note that, without the effects of PRD, spectral convolution alone should (and does) not impact the performance of the WFA in the case of a uniform magnetic field.

4. THE WFA APPLIED TO SYNTHETIC MG II SPECTRA EMERGING FROM AN ACTIVE REGION SIMULATION

In this section we analyze the diagnostic capabilities of the WFA when applied to Mg II lines emerging from an active region simulation, and in particular, how the accuracy of the WFA is affected by finite spectral resolution.

We start from a radiative magneto-hydrodynamic (rMHD) simulation of an active region (AR) from the MURaM code with the same setup as the one described in Rempel (2017). The simulation presents a small active region with a corona that is self-consistently heated by the Poynting flux resulting from photospheric magneto-convection. While the treatment of the chromosphere is simplified (grey RT and LTE ionization), Bjørgen et al. (2019) showed that synthetic chromospheric emission captures many observationally known features, at least on a qualitative level. The purpose of this simulation is not to provide an exact description of an active region chromosphere, but to provide a test case with known "ground truth" that samples the typical parameter space of an active region. The size of the horizontal domain is 98x98 $\rm Mm^2$ with a spatial sampling of 64 km in each horizontal direction. The vertical domain spans $\sim$ 49.1 Mm (sampled every 32 km), of which approximately $\sim$ 13.1 Mm lie below the surface (defined as the height where the average optical depth at 500 nm, τ_{500}, is unity). We select a small subset of the simulation box that encompasses a quarter of one of the sunspots and the strongly magnetized granulation surrounding it to synthesize the Mg II lines in the UV. Fig. 5 presents the physical variables of the simulation in the horizontal slice at h=0 km. The strong and almost vertical magnetic field at the center of the umbra (top right corner of each panel) decreases rapidly in strength towards the outer edge of the sunspot, where it also becomes almost horizontal.

We extract the physical quantities for each column (1D atmosphere) in the simulation and feed it to Hanle-RT to generate the Stokes spectra. Before feeding the atmospheres to Hanle-RT some pre-processing is necessary. Each column of the simulation is truncated 192 km below its $\tau_{500} = 1$ level. The relative shift between this level across individual atmospheres in the simulation domain can be as large as 800km due to the surface being very depressed at the center of the umbra compared to the surrounding granulation. The top of each atmosphere is also truncated

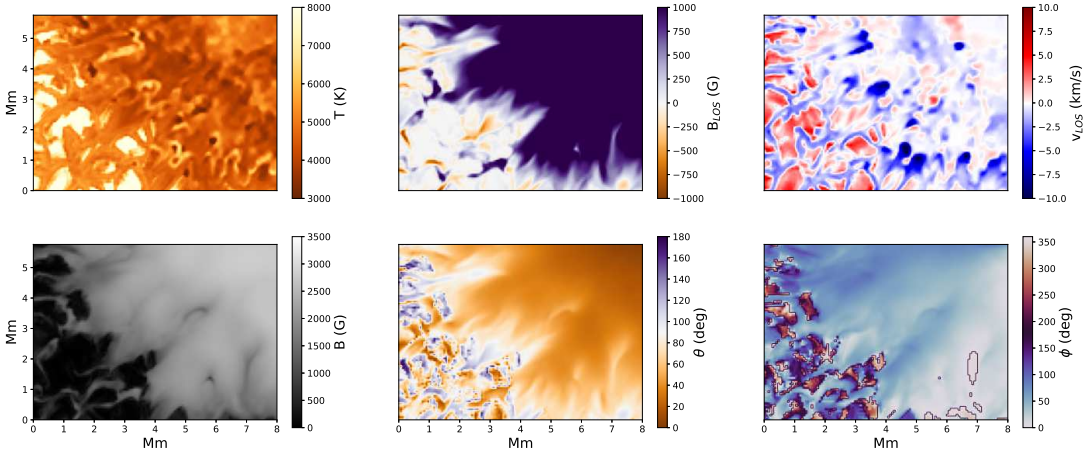

Figure 5. Physical parameters at h=0 km in the subset of the original MURaM simulation chosen for this study. From left to right and top to bottom: temperature, T, LOS component of the magnetic field, $B_{\rm LOS}$, LOS velocity, $v_{\rm LOS}$, magnetic field strength, B, its inclination with respect to the local vertical, θ, and its azimuth in the horizontal plane, ϕ).

at the location where the temperature reaches 10^5K, since the Mg II lines should form well below said temperature (Heinzel et al. 2014). The atmospheres are further simplified by removing the velocity field. Because there are no velocity gradients, the emerging spectra will be close to symmetric. This simplification is necessary for the purpose of isolating the effects of spectral resolution on the WFA inferences from further vertical smearing that the velocity gradients may introduce (although Centeno 2018, showed that moderate velocity gradients do not negatively impact WFA inferences of $B_{\rm LOS}$ from Ca II 8542 Å). Furthermore, an ad-hoc microturbulent velocity profile is added to each column's atmosphere. The latter is modeled as a linear function of height, ranging from 0 kms^{-1} at h=-192 km, to 7 kms^{-1} at the highest possible height (h=1856 km), so that it has qualitatively comparable values to those in the semi-empirical model atmosphere FALC, as well as in the inversion results of sunspot/plage IRIS spectra in de la Cruz Rodríguez et al. (2016). This high microturbulence value still produces spectra that are much narrower than those in Level 2 IRIS data, as shown in Fig 6.

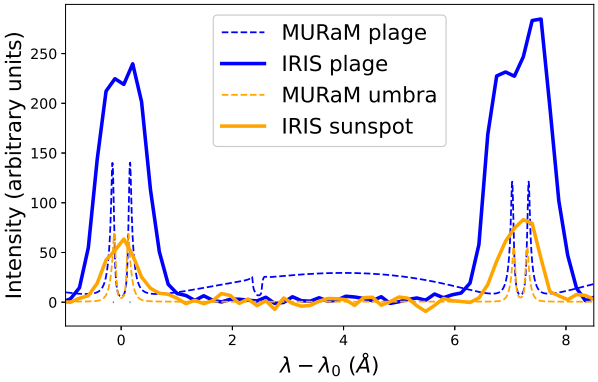

Figure 6. Dashed lines: averaged synthetic Mg II spectra over a 240x240 km^2 area in the top right (umbra) and bottom left ("plage") corners of the simulation box. For comparison, Level 2 IRIS spectra inside a sunspot and a plage area are shown with solid lines. Note that the individual synthetic spectra averaged for this figure were calculated at rest (no Doppler shift), and were not subjected to spectral degradation. Both of these factors contribute to them being narrower than the observed spectra. In this figure, the MURaM and the IRIS specific intensities were scaled arbitrarily.

The spectra are synthesized in the 3-term Mg II atom described above, for a disk center observing geometry (i.e. a heliocentric angle of 0°). Synthesizing the Mg II h&k lines plus the UV triplet in the 3-term atomic model with Hanle-RT is a computationally demanding exercise. The calculation of the atomic level polarization (population imbalances and quantum coherences amongst magnetic sublevels) as well as the treatment of the Mg II h&k doublet in PRD dramatically drive the increase in computing time compared to spectral line modeling without these effects. The median run time for generating a single spectrum is 10 core-hours (c-h), and synthesizing the 11,250 spectra in the FoV in Fig. 5 took a total 145,000 c-h on NCAR's Cheyenne supercomputer.

In the case of sunspots, magnetic fields are strong enough to significantly depolarize the atomic levels, leading to polarization signals that exhibit, almost typical, Zeeman patterns. In this regime, if the spectral lines are wide enough, the WFA can be a suitable tool for quantifying the magnetic field vector because the inference error induced by any residual atomic polarization can typically be ignored for the expected field strengths of active regions (Kuckein et al. 2009).

4.1. *Retrieval of $B_{\rm LOS}$ from Mg II h & k*

In this section we apply Eq. 3 to retrieve the LOS component of the magnetic field from Stokes I and V of the Mg II h and Mg II k lines separately, but first, we implement an automated algorithm that finds the wavelength range corresponding to the inner lobes of Stokes V based on the position of its peaks (which appear as zero-crossings in the first derivative of Stokes V with respect to wavelength). Even in the absence of velocities, the shape of the spectral line changes significantly across the FoV, and a single pre-chosen wavelength interval is not adequate to exclude the outer Stokes V lobes in all the spectra.

After finding the desired wavelength interval, we carry out a linear fit between the left- and the right-handsides of Eq. 3, in the same way as in Section 3, for each set of Stokes I and V emerging from the FoV of the simulation box. Fig. 7 shows density scatter plots of the retrieved $B_{\rm LOS}$ from Mg II k (left) and Mg II h (middle) against the MURaM model values. The latter are taken at the height where each line center reaches optical depth unity ($\tau_{\rm h}$ or $\tau_{\rm k}$ = 1). This is taken as a representative height for comparison with the model values, however, the emergent spectra are sensitive to a range of heights over which the magnetic field is not constant. The gradient of the magnetic field around the region of formation of the lines is responsible for the scatter in the WFA inferences. The magnetic field bin size is 40 G, and the darkness of the gray-scale is proportional to the number of samples in the bin. The red line represents the ideal solution (if the WFA yielded exactly the model value). From these figures it is clear that the WFA does a good job at retrieving the LOS component of the magnetic field up to LOS field strengths of $B_{\rm LOS} \sim 1000$ G. Beyond this value, the WFA starts to systematically overestimate $B_{\rm LOS}$. This is due the fact that we are entering the strong field regime in which the WFA is no longer valid, according to the requirement of Eq. 1. Note that the validity of the weak field regime hinges on the value of B, not of $B_{\rm LOS}$. A LOS component of 1000 G necessarily entails a field strength larger or equal to that. The right panel of Fig. 7 presents the relative error incurred by the WFA when applied to the Mg II k line as a function of the total field strength, B, in the model. This panel clearly shows that the systematic deviation of the WFA results towards larger values starts around $B \sim 1500$ G. Fig. 8 shows the values of $\bar{g}\Delta\lambda_B/\Delta\lambda_D$ for the Mg II k line as a function of height in one of the 1D MURaM atmospheres, for four different (uniform) magnetic field strengths. Around 1500 G, the Mg II k line no longer satisfies the WFA condition. This threshold varies from one atmosphere to another, since meeting or not the condition depends on the temperature and the microturbulent velocity as well as the magnetic field strength.

4.2. *Effects of spectral resolution on the retrieval of $B_{\rm LOS}$*

In order to understand the effects of a finite spectral resolution on the WFA inferences, we convolve the spectra emerging from the simulation with gaussian PSFs of different widths.

Fig. 9 shows scatter plots of the WFA inference against the corresponding model value for the cases of "infinite" spectral resolution (left), R = $\Delta\lambda/\lambda$ =45,000 (middle) and R = 30,000 (right). The red line represents the one-to-one solution while the blue line shows a linear regression of the data points in each scatter plot. As discussed earlier, the WFA tends to over-estimate the field above $B_{\rm LOS} = 1000$ G in the spectrally resolved case (left panel). As the value of R decreases, the method starts to underestimate $B_{\rm LOS}$, counteracting the effect of the WFA inaccuracy in the strong field regime. This systematic bias towards lower fields (seen in the middle and right panels) cannot be attributed to the core of the line sensing lower atmospheric layers due to spectral smearing (i.e. along the LOS) mixing. Spectral information probing lower atmospheric layers would typically lead to a bias towards larger inferred field strengths, not

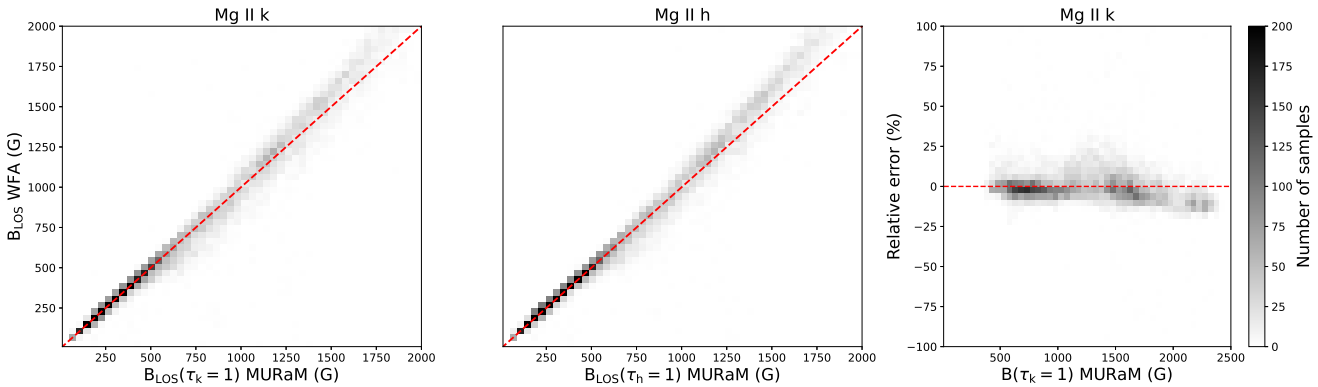

Figure 7. Scatter density plots of the retrieved value of B_{LOS} (y-axis) against their model counterparts where $\tau_{LINE} = 1$ (x-axis) for Mg II k (left) and h (middle). The darker the grey-level, the higher the number of samples in the bin. The bin size is 40 G. The red line represents the ideal solution, if the WFA retrieved exactly the model value. The panel on the right shows the relative error incurred by the WFA applied to Mg II k as a function of the magnetic field strength in the MURaM model.

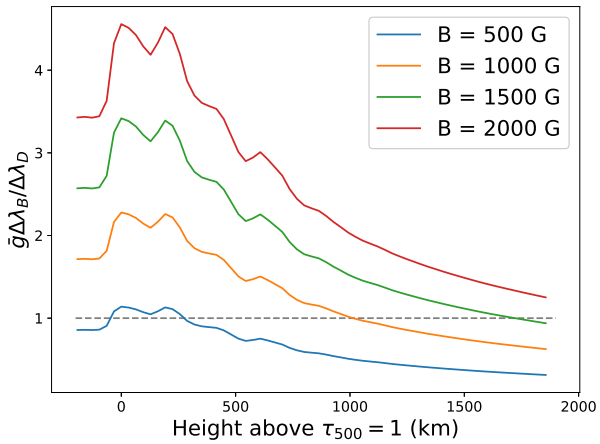

Figure 8. Meeting the WFA condition. The lines show the value of $\bar{g}\Delta\lambda_B/\Delta\lambda_D$ for the Mg II k line in one of the MURaM atmospheres, where the magnetic field has been replaced by a uniform one a function of height. Three different magnetic strength values are considered, showing that, at the typical height of formation of the Mg II lines, a field of 1500 G no longer meets the condition of Eq. 1.

weaker, because there is an almost monotonic decrease of the magnetic field strength as a function of height across the entire FoV of Fig. 5. This points to PRD effects being brought into the core of the line due to spectral smearing and thus impacting (decreasing) the WFA inferences, which should otherwise increase with spectral mixing (i.e. mixing along the line-of-sight). The larger the value of R, the greater the impact on the inferred B_{LOS}.

4.3. *Retrieval of B_T through the WFA*

The retrieval of the transverse magnetic field through the WFA relies on Eqs. 4 and 5. While Eq. 4 is applicable far away from the central wavelength of the spectral line, λ_0, Eq. 5 is technically valid only in the core. For this reason alone, the former can only be used to sample lower atmospheric layers from the wings of the Mg II lines, whilst the latter should be able to probe the transverse component of the magnetic field in the higher layers of the atmosphere. A practical caveat to both relations is that, when the magnetic field is very weak, the linear polarization signals tend to be dominated by scattering polarization, the Hanle effect, and magneto-optical effects, rendering the WFA a useless tool in these cases. The magnetic field needs to reach a few hundred gauss in strength in order to significantly depolarize the atomic energy levels of the upper level of the Mg II UV doublet, and allow the linear polarization signals to enter

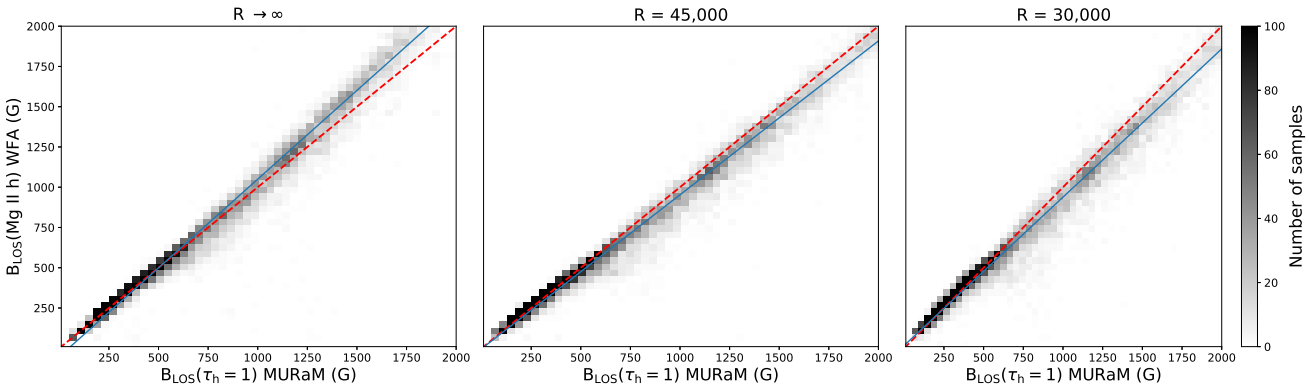

Figure 9. Scatter density plots of the retrieved value of B_{LOS} retrieved from Mg II h against their model counterparts for the case of infinite spectral resolution (left), R = 45,000h (middle) and R = 30,000 (right). The model values are taken at the height where the core of each line reaches optical depth unity. The darker the grey-level, the higher the number of samples in the bin. The bin size is 40 G. The red line represents the ideal solution and the blue line shows a linear fit through the data. The left panel in this figure shows the same data than the middle panel of Fig. 7

the Zeeman-dominated regime, where the WFA is valid. In the case at hand, the weakest magnetic field in the entire FoV is still ≈ 500 G at the top of the atmosphere[3].

Since the retrieval of the magnetic field at the top of the chromosphere is of most interest to this exercise, we will focus on testing the accuracy of the WFA through Eq. 5. Three different applications of this equation are tested within the core of the line, here defined as the wavelength range occupied by the inner lobes of Stokes V. Method #1 performs a standard linear regression of the left and right handsides of Eq. 5. In the linear regression analogy described in Section 3, y_i now corresponds to L_λ, while x_i takes the values of $1/4C_T|d^2I_\lambda/d\lambda^2|$. The slope of the fit corresponds to $B_{\rm T}^2$, while the intercept should be close to zero if the model represents the data adequately. In method #2, the intercept b is forced to be zero and only the slope is fitted, which results in the following expression for the linear regression:

$$B_{\rm T}^2 = \frac{4}{C_{\rm T}} \frac{\sum_\lambda (\left|\frac{\partial^2 I_\lambda}{\partial \lambda^2}\right| L_\lambda)}{\sum_\lambda \left(\frac{\partial^2 I_\lambda}{\partial \lambda^2}\right)^2} \tag{6}$$

In method #3, we calculate the wavelength-average of the left- and the right-hand sides of Eq. 5 and obtain $B_{\rm T}^2$ as the ratio between the two:

$$B_{\rm T}^2 = \frac{4}{C_{\rm T}} \frac{\sum_\lambda L_\lambda}{\sum_\lambda \left|\frac{d^2 I_\lambda}{d\lambda^2}\right|} \tag{7}$$

Additionally, we test the application of Eq. 13 in Martínez González et al. (2012) (method #4). This approach, estimates the magnetic field vector by minimizing a merit function that explicitly uses Stokes Q and U, instead of L. This results in the following equation to obtain B_T:

$$B_T^2 = \frac{4}{C_{\rm T}} \frac{\sqrt{\sum_\lambda (Q_\lambda \frac{\partial^2 I_\lambda}{\partial \lambda^2})^2 + \sum_\lambda (U_\lambda \frac{\partial^2 I_\lambda}{\partial \lambda^2})^2}}{\sum_\lambda (\frac{\partial^2 I_\lambda}{\partial \lambda^2})^2} \tag{8}$$

Fig. 10 shows the results of applying the WFA to Mg II h for inferring the transverse component of the field from the synthetic spectra using these four different methods (from left to right, the columns correspond to methods #1, #2, #3 and #4, respectively). Each panel presents a density scatter plot of the retrieved transverse magnetic field against its model counterpart at the height where $\tau_{\rm MgIIh} = 1$. The three rows show the results for different spectral resolutions, R.

Let's take a look at the first row of results, for the spectrally resolved case. The first and second panels show the WFA results from the linear regressions of Eq. 5 with and without intercept, respectively (methods #1 and #2). We find that, fixing the intercept to zero yields slightly more accurate results than allowing it to be a free parameter in

[3] The top of the atmosphere in this context is defined by the height at which the temperature reaches 10^5 K

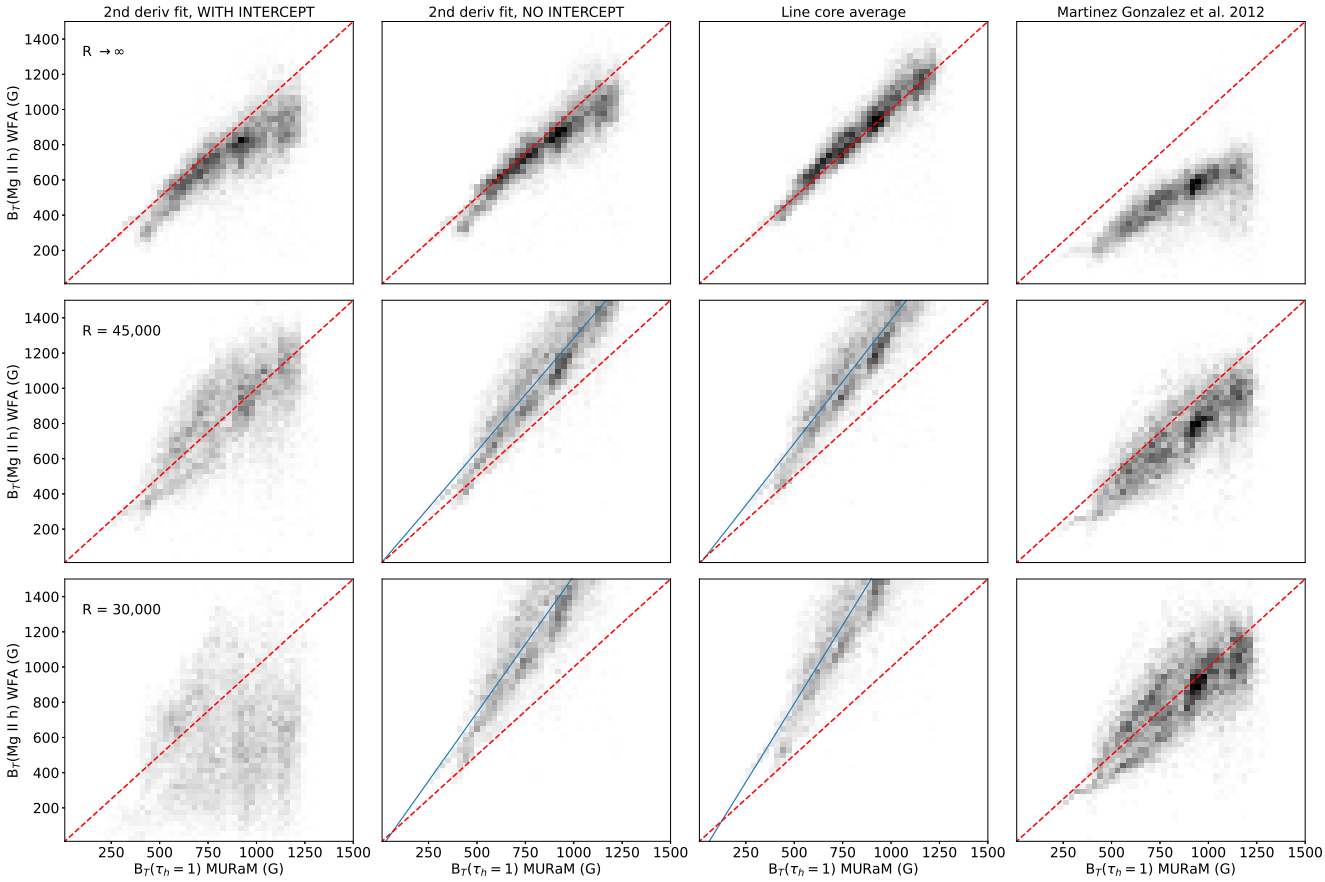

Figure 10. Scatter density plots of the values of B_T retrieved from Mg II h against their model counterparts for the case of infinite spectral resolution (top row), R = 45,000h (middle row) and R = 30,00 (bottom row). The four columns correspond to retrieval methods #1, #2, #3 and #4 respectively, described in the manuscript text. The darker the grey-level, the higher the number of samples in the bin. The bin size is 40 G and the color scale is the same for all panels. The red line represents the ideal solution if the WFA inference were perfect, while blue lines show linear fits through the scatter plot data.

the regression. This is a symptom of the WFA model not representing the data accurately (i.e. the best linear fit does not naturally cross the origin). The third panel shows the case where the linear fit is forgone and only a ratio of the wavelength-averaged quantities is used. The accuracy is comparable to that of the previous methods. The last panel shows the results from the application of Eq. 8, which systematically underestimates the values of B_T.

As we decrease the spectral resolution to 45,000 (middle row) and 30,000 (bottom row) we find that the accuracy of all methods degrades, with method #1 losing all correlation and retaining no diagnostic value at R = 30,000. Methods #2 and #3 show very similar behaviors as the spectral resolution worsens. They both result in an increased spread of the WFA solution around the model value, and they over-estimate the transverse field by a larger amount the poorer the resolution. The spectral smearing is bringing information from the line wings into the core and "contaminating" the WFA inferences. This over-estimate is partly due to the fact that the wings of the line sense lower layers (and therefore stronger fields). The impacts of PRD effects and scattering polarization in the line wings could also be contributing to the error. From the setup of this particular experiment it is impossible to quantify the relative contributions of each one of these effects. In any case, this over-estimate is relatively well behaved (systematic as a function of field strength) and could be corrected with a proper calibration of the WFA inferences [4]. The blue lines in these panels show a linear fit through the scatter plot data, suggesting that a simple linear correction to the WFA inference could bring it closer to the real B_T value. Method #4 also results in an increased spread with systematically larger inferred values as we degrade the resolution.

[4] This may be MHD model-dependent, in which case may only be done when MHD models are able to reproduce the observed spectra.

It is worth noting that, while the amplitudes of the linear polarization signals emerging from the AR simulation reach values of the order of 1% of the continuum intensity, we might expect them to be much smaller in real observations, challenging the detection of Stokes Q and U signals above typical observational noise levels. A brief analysis of the effects of noise is shown in the Appendix.

5. CONCLUSIONS

We study the impact of finite spectral resolution on the retrieval of magnetic field quantities from the Mg II h&k lines through the weak field approximation.

First, we look at the case of the WFA applied to synthetic Mg II spectra emerging from a semi-empirical FAL-C model atmosphere with an ad hoc uniform magnetic field with a LOS component of 141 G. Eq 3 is applied to the spectrally resolved case in two wavelength ranges: one that contains only the inner lobes of Stokes V and one that encompasses the outer lobes as well. We find that the error in the retrieval of $B_{\rm LOS}$ jumps from 1.4% in the case of the narrower wavelength range, to -13% when the outer lobes are considered (left panels of Fig. 2). The results remain almost identical when the spectra are synthesized without magneto-optical effects. It is only when PRD is turned off that the WFA inferences in the two spectral ranges agree and yield the smallest error (0.2%), confirming the results from del Pino Alemán et al. (2016). It is well know than PRD effects affect much more prominently the wings than the line core (Leenaarts et al. 2013a,b), and we speculate that the correction to the emissivity term due to PRD is purely responsible for the WFA breaking down.

Broad spectral point spread functions have the effect of spectral mixing, bringing information from the line wings into the core and vice-versa. We degrade the data spectrally by convolving them with gaussian PSFs of different widths that emulate various spectral resolutions. We find that, when we apply the WFA to the inner lobes of Stokes V in the degraded spectra, a larger error ensues. By repeating the experiment turning off PRD effects, we show that the latter are purely responsible for the inference errors, as the spectral smearing brings information from the line wings into the inner wavelength range around the core of the line. Fig. 4 shows the inaccuracy of the inferred of $B_{\rm LOS}$ as a function of spectral resolution. The relative error decreases with increasing spectral resolution, from $\sim 12\%$ for R = 30,000 to $\sim 3\%$ for R = 90,000.

In order to test this effect in a more diverse set of atmospheres, we synthesize the Mg II h&k spectra emerging from a rMHD simulation of an active region from the MURaM code. We select a portion of the simulation box that contains a quadrant of a sunspot and the strongly magnetized granulation surrounding it. When Eq. 3 is applied to the inner lobes of Stokes V, both Mg II h and Mg II k deliver remarkably accurate results for most pixels in the FoV, when comparing the retrieved value of the LOS component of the magnetic field to the model value at $\tau_{\rm LINE} = 1$. The WFA inference starts to deviate significantly from the model value starting at a magnetic field strength of ~ 1500 G (right panel of Fig. 7), due to a departure from the weak field regime. Both spectral lines deliver quantitatively comparable results. The effect of a reduced spectral resolution results in the WFA underestimating the LOS magnetic field when compared to the spectrally resolved case. We justify that this bias is due to PRD effects being transported into the line core due to spectral smearing, rather than a result of sensing lower atmospheric layers due to line-of-sight mixing.

The extraction of the transverse component of the magnetic field through Eq. 5 was tested subsequently in the line core (defined here as the region spanned by the inner lobes of Stokes V). We find that performing a linear regression of the left and right handsides of the equation yields better results when the intercept is forced to be zero than when it is a free parameter of the fit (see first and second panels of the top row of Fig. 10). This is because the WFA model does not reproduce the behavior of the data with fidelity. A simple ratio of the wavelength averages of the left and right sides of Eq. 5 (third panel of the top row) delivers equally good results, while Eq. 8 results in systematically lower inferences of $B_{\rm T}$ (fourth panel of the top row). Degrading the spectral resolution results in a systematic over-estimate of the retrieved $B_{\rm T}$, which grows with decreasing value of R. The precision of the estimate also worsens (see the increased spread in the scatter plots of Fig. 10), yielding method #1 useless in the case of R=30,000. For methods #2 and #3 , the systematic offset of the WFA retrieval could be calibrated with a simple linear fit.

One big caveat to the WFA is that the method does not shed information on the atmospheric heights of the retrieved magnetic quantities. The WFA inferences will correspond to weighted averages around the height of formation of the spectral window that is used (typically the line core). Across the domain of the MURaM simulation used in this work, the geometric height of formation of the Mg II cores varies by ≈ 1.4 Mm, being very depressed at the center of the umbra and a lot higher in the quieter areas. A similar variation is expected for the heights probed by the WFA.

This could pose a problem for extrapolations of the vector magnetic field inferred from observations, especially in the absence of further modeling that constrains the height probed by the WFA.

It is interesting to note that synthesizing the Mg II spectra in a simulation box featuring 11,250 1D realizations of the atmospheric properties took 145,000 core-hours on NCAR's Cheyenne supercomputer. This highlights one of the difficulties of interpreting the Mg II polarization spectra (and other chromospheric resonance lines). The forward modeling alone is computationally expensive, and traditional inversion methods based on merit function minimization schemes tend to require many calls of the forward model until the synthetic profiles converge to the observations, limiting the use of this approach. That is why there are several ongoing explorations of machine-learning based inversion algorithms, or of model parameterizations that can significantly reduce the number of forward-model iterations. Physical approximations such as the WFA remain valuable to render the magnetic field retrieval tractable.

In conclusion, the WFA can be applied to the Mg II h&k lines emerging from strong field regions (sunspots and strongly magnetized surroundings), but one has to be aware of the systematic impacts that finite spectral resolution has on the inferences.

APPENDIX

The magnetic field inferences through the WFA must be impacted by photon noise in the observations, resulting not just in uncertainties, but also in systematic biases (Martínez González et al. 2012; Centeno 2018). Even though it is beyond the scope of this work to study the effects of noise in detail, we briefly evaluate the relative merits of the different methods used in Section 4.3 for the inference of $B_{\rm T}$ when gaussian noise is applied to the spectra. To quantify the effects of noise we add wavelength-independent gaussian noise to Stokes I, Q, U and V and repeat the WFA inferences for the spectrally resolved case. Three different signal-to-noise ratios (SNR) are considered, $SNR = I_{\rm C}/\sigma = [\infty, 1000, 100]$, where the reference signal, $I_{\rm C}$, is the pseudo-continuum intensity 3.3 Å blue-wards of Mg II k, and σ is the standard deviation of the noise.

Figure 11 shows the WFA inferences of $B_{\rm T}$ from Mg II h for the noiseless case in the top row (which is the same as the top row of Fig.10), for $SNR = 1000$ in the middle row, and $SNR = 100$ in the bottom row. While for a $SNR = 1000$ the results are still robust, a $SNR = 100$ not only increases the spread of the inferences around the ideal solution, but also introduces systematic biases in almost all of the cases. While method #1 (linear fit of Eq. 5 with free-fitting intercept) tends to experience a systematic bias towards lower inferred values of $B_{\rm T}$, methods #2 and #3 are affected in the opposite direction, with a tendency to overestimate $B_{\rm T}$. Method #4 also experiences a bias towards larger inferred values, but is less dramatically affected than the previous two methods.

The inference of $B_{\rm LOS}$ is not affected by the noise levels tested above. Because the amplitude of Stokes V across the FoV of the simulation domain is large, even a SNR=100 renders circular polarization signals significantly above the noise level, retaining their diagnostic power with little to no negative impacts.

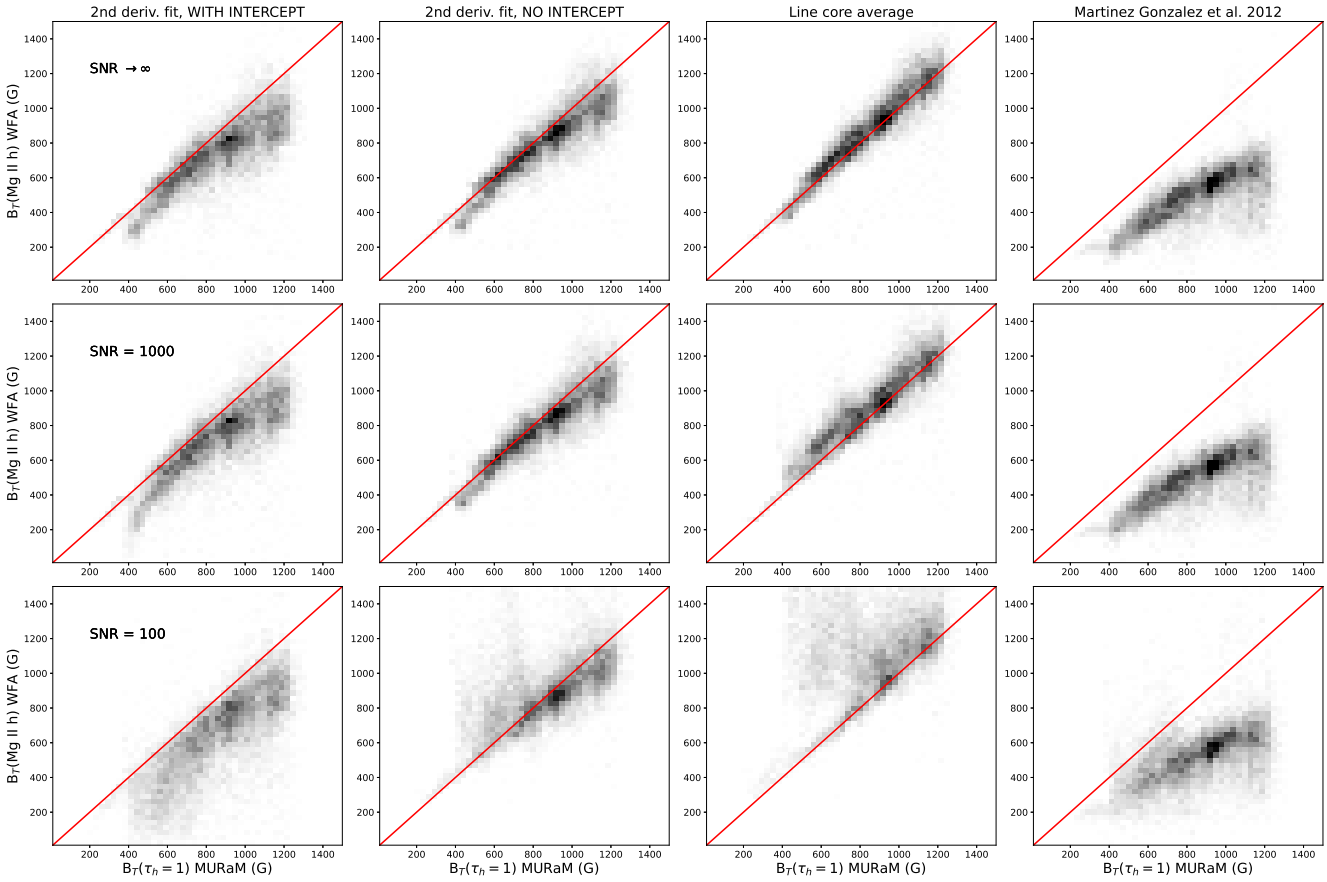

Figure 11. Scatter density plots of the values of B_T retrieved from Mg II h against their model counterparts for three different SNR values: SNR $\to \infty$ (top row), SNR = 1000 (middle row) and SNR = 100 (bottom row). The four columns correspond to retrieval methods #1, #2, #3 and #4 respectively, described in the manuscript text. The darker the grey-level, the higher the number of samples in the bin, which is 40 G in width. The color scale is kept constant across all panels. The red line represents the one-to-one correspondence.

This material is based upon work supported by the National Center for Atmospheric Research, which is a major facility sponsored by the National Science Foundation under Cooperative Agreement No. 1852977. We would like to acknowledge high-performance computing support from Cheyenne (doi:10.5065/D6RX99HX) provided by NCAR's Computational and Information Systems Laboratory, sponsored by the National Science Foundation. T.d.P.A. acknowledges the funding received from the European Research Council (ERC) under the European Union's Horizon 2020 research and innovation programme (ERC Advanced Grant agreement No 742265).

REFERENCES

Alsina Ballester, E., Belluzzi, L., & Trujillo Bueno, J. 2016, ApJL, 831, L15

Bjørgen, J. P., Leenaarts, J., Rempel, M., et al. 2019, A&A, 631, A33

Bohlin, J., Frost, K., Burr, P., Guha, A., & Withbroe, G. 1980, SoPh, 65, 5

Casini, R., del Pino Alemán, T., & Manso Sainz, R. 2017, ApJ, 835, 114

Casini, R., Landi Degl'Innocenti, E., Landolfi, M., & Trujillo Bueno, J. 2002, ApJ, 573, 864

Casini, R., & Manso Sainz, R. 2016, ApJ, 824, 135

Centeno, R. 2018, ApJ, 866, 89

Centeno, R., de la Cruz Rodríguez, J., & del Pino Alemán, T. 2021, ApJ, 918, 15

Centeno, R., Trujillo Bueno, J., & Asensio Ramos, A. 2010, ApJ, 708, 1579

de la Cruz Rodríguez, J., Leenaarts, J., & Asensio Ramos, A. 2016, ApJL, 830, L30

De Pontieu, B., Title, A. M., Lemen, J. R., et al. 2014, SoPh, 289, 2733

del Pino Alemán, T., Casini, R., & Manso Sainz, R. 2016, ApJL, 830, L24

Fontenla, J. M., Avrett, E. H., & Loeser, R. 1990, ApJ, 355, 700

Heinzel, P., Vial, J. C., & Anzer, U. 2014, A&A, 564, A132

Ishikawa, R., Bueno, J. T., del Pino Alemán, T., et al. 2021, Science Advances, 7, eabe8406

Judge, P., Rempel, M., Ezzeddine, R., et al. 2021, ApJ, 917, 27

Kleint, L. 2017, ApJ, 834, 26

Kosugi, T., Matsuzaki, K., Sakao, T., et al. 2007, SoPh, 243, 3

Kriginsky, M., Oliver, R., Antolin, P., Kuridze, D., & Freij, N. 2021, A&A, 650, A71

Kuckein, C., Centeno, R., Martínez Pillet, V., et al. 2009, A&A, 501, 1113

Lagg, A., Lites, B., Harvey, J., Gosain, S., & Centeno, R. 2017, SSRv, 210, 37

Landi Degl'Innocenti, E., & Landi Degl'Innocenti, M. 1973, SoPh, 31, 299

Landi Degl'Innocenti, E., & Landolfi, M. 2004, Polarization in Spectral Lines, Vol. 307, doi:10.1007/978-1-4020-2415-3

Leenaarts, J., Pereira, T. M. D., Carlsson, M., Uitenbroek, H., & De Pontieu, B. 2013a, ApJ, 772, 89

—. 2013b, ApJ, 772, 90

Li, H., del Pino Alemán, T., Trujillo Bueno, J., & Casini, R. 2022, arXiv e-prints, arXiv:2205.15666

Libbrecht, T., de la Cruz Rodríguez, J., Danilovic, S., Leenaarts, J., & Pazira, H. 2019, A&A, 621, A35

Lites, B. W., Akin, D. L., Card, G., et al. 2013, SoPh, 283, 579

Manso Sainz, R., del Pino Alemán, T., Casini, R., & McIntosh, S. 2019, ApJL, 883, L30

Martínez González, M. J., Manso Sainz, R., Asensio Ramos, A., et al. 2015, ApJ, 802, 3

Martínez González, M. J., Manso Sainz, R., Asensio Ramos, A., & Belluzzi, L. 2012, MNRAS, 419, 153

Merenda, L., Trujillo Bueno, J., Landi Degl'Innocenti, E., & Collados, M. 2006, ApJ, 642, 554

Morosin, R., de la Cruz Rodríguez, J., Vissers, G. J. M., & Yadav, R. 2020, A&A, 642, A210

Pereira, T. M. D., Leenaarts, J., De Pontieu, B., Carlsson, M., & Uitenbroek, H. 2013, ApJ, 778, 143

Pesnell, W. D., Thompson, B. J., & Chamberlin, P. C. 2012, SoPh, 275, 3

Rempel, M. 2017, ApJ, 834, 10

Sainz Dalda, A., de la Cruz Rodríguez, J., De Pontieu, B., & Gošić, M. 2019, ApJL, 875, L18

Scherrer, P. H., Schou, J., Bush, R. I., et al. 2012, SoPh, 275, 207

Shchukina, N. G., & Trujillo Bueno, J. 2019, A&A, 628, A47

Siu-Tapia, A. L., Bellot Rubio, L. R., Orozco Suárez, D., & Gafeira, R. 2020, A&A, 642, A128

Solanki, S. K., del Toro Iniesta, J. C., Woch, J., et al. 2020, A&A, 642, A11

Trujillo Bueno, J., Landi Degl'Innocenti, E., & Belluzzi, L. 2017, SSRv, 210, 183

Vissers, G. J. M., Danilovic, S., de la Cruz Rodríguez, J., et al. 2021, A&A, 645, A1